Non-Periodic Epsilon-Near-Zero Metamaterials at Visible Wavelengths for Efficient Non-Resonant Optical Sensing

Zelio Fusco[a], Mahdiar Taheri[b], Renheng Bo[a], Thanh Tran-Phu[a], Hongjun Chen[a], Xuyun Guo[c], Ye Zhu[c], Takuya Tsuzuki[b], Thomas P. White[d], and Antonio Tricoli[a]

[a] Nanotechnology Research Laboratory, College of Engineering and Computer Science, The Australian National University, ACT 2601, Australia
[b] Laboratory of Advanced Nanomaterials for Sustainability, College of Engineering and Computer Science, The Australian National University, ACT 2601, Australia
[c] Department of Applied Physics, The Hong Kong Polytechnic University, Hong Kong
[d] Research School of Electrical, Energy and Materials Engineering, The Australian National University, ACT 2601, Australia

Abstract

Epsilon-near-zero (ENZ) materials offer unique properties for applications including optical clocking, nonlinear optics and telecommunication. To date, the fabrication of ENZ materials at visible wavelengths relies mostly on the use of periodic structures, providing some manufacturing and material challenges. Here, we present the engineering of non-periodic sodium tungsten bronzes (Na_xWO_3) metamaterials featuring ENZ properties in the visible spectrum. We showcase their use as efficient optical sensors demonstrating a non-resonant sensing mechanism based on refractive index matching. Our optimized ENZ metamaterials display an unconventional blue-shift of the transmittance maximum to increasing refractive index of the surrounding environment, achieving sensitivity as high as 150 nm/RIU. Our theoretical and experimental investigations provide first insights on this sensing mechanism establishing guidelines for the future engineering and implementation of efficient ENZ sensors. The unique optoelectronic properties demonstrated by this class of tuneable Na_xWO_3 materials bear potential for various applications ranging from light-harvesting to optical photodetectors.

Keywords

Epsilon-near-zero, non-periodic, metamaterials, sensing, non-resonant, sodium-tungsten-bronzes

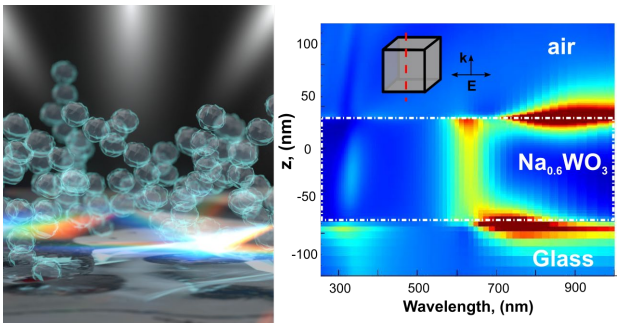

Introduction

Optically resonant subwavelength metasurfaces based on the collective oscillations of conduction electrons in nanostructured metals, i.e. surface plasmons, [1] enable confinement and enhancement of the electromagnetic energy in subwavelength regions,[2] allowing efficient optical bio- and chemical-sensing[3-5]. In the past decades, engineering of nanostructured metal metasurfaces has significantly increased the sensitivity of plasmonic sensors achieving down to single molecule detection limits[6-9]. However, the high intrinsic losses at visible frequencies of established plasmonic materials –arising from the high imaginary part of the permittivity, ε''– determine a threshold for the operating frequencies of these materials[10, 11] (Supplementary Information, Appendix A).

To overcome the above limitations, some non-resonant approaches have been recently proposed for refractive index sensing. The latter include the introduction of optical modulation in Mach-Zehnder interferometers via channel waveguide,[12] layered metal-insulator-metal structures,[13] or spatial mapping of the scattering field intensity.[14] While providing benefits, these methodologies often require a larger footprint than plasmonic metasurfaces due to the large path length requirements.[15] An alternative route is provided by engineering the metamaterials dielectric function to achieve vanishing real part of the permittivity, a condition referred to as epsilon-near-zero (ENZ).[16] ENZ conditions commonly occur in the vicinity of the plasma resonance, at the cross-over frequency (λ_c), where the real part of the permittivity, ε', turns from negative to positive.[17] As λ_c depends on the carrier concentration, n, metallic nanomaterials (n~10^{23} cm^{-3}) exhibit ENZ properties in the UV region of the spectrum, while transparent conductive oxides, featuring a smaller carrier concentration (n~10^{20} cm^{-3}), achieve ENZ in the infra-red spectrum.[18]

Early application of ENZ materials have been recently demonstrated with nano-optical circuits,[19] photon-funnels,[20] invisibility cloaking[21] and nonlinear optics.[22] Realization of ENZ materials at visible wavelengths is a challenging task,[23-25] even more so with non-periodic disordered structures. Even elevated levels of doping in transparent conductive oxides and semiconductors are insufficient to shift this region below near-infrared wavelengths[18, 26]. To date, achieving ENZ metamaterials at visible frequencies has relied on the fabrication of resonant subwavelength arrays[27] and structured alternate layers.[23] These top-down approaches impose limitations on materials and fabrication techniques, restricting the practical application of visible spectrum ENZ metamaterials. The engineering of disordered materials displaying ENZ properties at visible wavelengths bears significant potential for numerous optoelectronic applications, including wavefront shaping[28] and light tunnelling.[29]

Here, we report the design and engineering of non-periodic ENZ metamaterials at visible wavelengths by large-scale self-assembly of sodium tungsten bronze (Na_xWO_3) nanocrystals. We demonstrate a first use of these ENZ metamaterials by fabrication of efficient optical sensors relying on a novel non-resonant sensing mechanism. These metamaterials demonstrate sensitivity as high as 150 nm/RIU for the detection of local refractive index variations. Our simulations and experiments reveal that this behaviour is largely insensitive to structural parameters such as nanostructure size, shape and distribution. Combined *ab-initio* and FDTD simulations of the Na_xWO_3 optoelectronic properties show a metal-to-insulator (MIT) transition, which is responsible for the minimization of the scattering cross-section and ENZ regime at visible wavelengths. We believe that these novel insights provide guidelines for the engineering of a family of optical ENZ materials with applications extending from sensing to photo-electrochemistry, non-linear photonics and optical cloaking.

Results and Discussion

Sodium tungsten bronze is an inorganic non-stoichiometric compound with a perovskite ABO_3 crystal structure (see Supplementary Information S1). It features extreme tuneability of its electronic band structure displaying a transition from insulator to conductor with varying Na content[30]. Recently, engineering of Na_xWO_3 structure has enabled to impart superconductivity[31], near-infrared absorption[32], photocatalytic[33], thermoelectric[34] and plasmonic propert*ies*[35-37]. While a range of routes have been proposed for the synthesis of Na_xWO_3,[32, 38 39] they mostly result in a broad size distribution of micrometre-scaleparticles, limiting the control on the optical properties (e.g. light scattering) of the resulting Na_xWO_3 films.

Here, we report the engineering of nanostructured Na_xWO_3 metamaterials with tuneable optolectronic properties by a rapid two-step approach. First, we synthesize a continuous aerosol of Na-doped WO_3 nanoparticles (with atomic Na/W ratio from 0 to 1) by flame spray combustion to achieve a direct self-assembly of these matarials onto quartz substrates, as shown in Figure 1a. This results in a ultraporous nanoparticle network (Figure 1c) with a thickness of ~5.1 μm. The latter thickness is independent of the Na amount (Na from 0 to 1) and show a similar hierarchical film porosity, charateristic of diffusion-limited aggregation[40, 41] (Figure S6) .

In a second step, Na_xWO_3 nanocrystals are formed by intercalation of Na in the WO_3 lattice during reduction of the as-deposited Na-doped WO_3 films at 800 °C in N_2 atmosphere with a 5% H_2 for 3 hours (Figure 1b). During the high temperature reduction, the porous Na-doped WO_3 nanoparticle network structure undergoes significant densification, accompanied by the formation of larger crystals with increasing sodium content (Figure 1d and Supplementary S5). Increasing the Na/W ratio lattice from 0 to 1 also led to a change in the crystal symmetry from monoclinic to orthorhombic, tetragonal and finally cubic.[30] This rich phase diagram is accompanied by a remarked colour change from black of the reduced WO_3 to the goldenish of $NaWO_3$ (Figure 2a) and are caused by a metal-to-insulator transition[42] where a sodium doping fraction of x~0.25 sets the threshold of the MIT. This provides a facile, morphology-independent, route to tune the Na_xWO_3 optoelectronic properties, as systematically shown by Tegg et al. in a series of theoretical analysis on this material.[35-37] Direct characterization of the permittivity of the Na_xWO_3 samples as a function of the Na concentration of Na should be attempted in the future (e.g. by ellipsometry) to provide further insight on the ENZ tenability of this material.

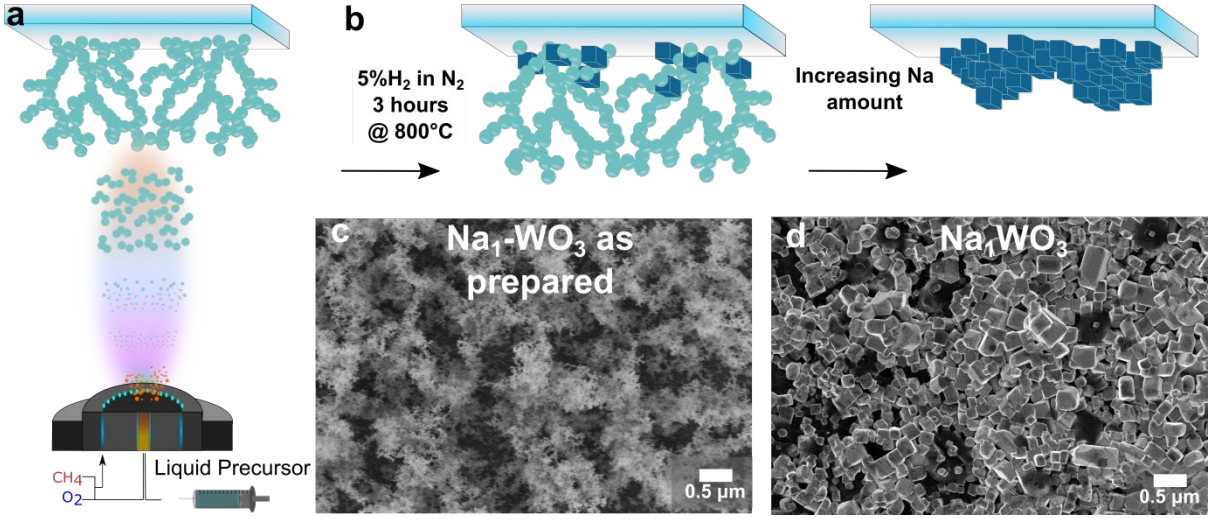

Figure 1. a) A hot aerosol of Na-doped WO_3 nanoparticles is continuously generated by flame spray pyrolysis of sodium and tungsten precursor solutions. b) Na_xWO_3 nanocrystals are obtained in a subsequent reduction step at 800 °C with a reducing atmosphere of 5% H_2 in N_2. c-d) Scanning electron microscope (SEM) micrographs of as-deposited Na-doped WO_3 (Na/W ratio of 1) before and after the thermal reduction process.

To provide further insights on the optoelectronic properties of these Na_xWO_3 nanocrystals, we performed first-principle *ab initio* simulations on the two case limit, namely a Na/W ratio of 0 (pure WO_3), representing the most semiconducting state, and of 1 ($NaWO_3$), representing the most metallic state. Figure 2b-c and Figure 2d-e show the computed band structure for a cubic Brillouin zone and the density of states (DOS) between -10 < Fermi Energy (E_F) < +10 eV for these Na/W ratio, respectively. Qualitatively, the overall electronic band structure and DOS are similar for both Na/W ratios. Their valence band structure is comprised of O 2p orbitals, while their conduction band is formed by W 5d and O 2p hybrids, in line with previous theoretical studies[35, 43]. The main difference between the WO_3 and $NaWO_3$ is related to the position of their Fermi energy, E_F. As the Na donates its 3s electrons to the W 5d orbitals, E_F rises with increasing Na content, intersecting the conduction band for a Na//W ratio > 0.25, which results in a metallic behaviour[44].

The computed band diagrams provide information about the electronic transition and resulting optical properties.[10] In particular, in every metallic system (Na_xWO_3 with x > 0.25), the interband transitions between valence and conduction bands have energies within the range ~ 3-8 eV that are well above the visible range. In contrast, the free carrier contribution (intraband transitions) to the imaginary part of the dielectric function falls in the visible spectrum with energy in the range of ~1-3 eV.

Figure 3a shows the results of electron energy loss spectroscopy (EELS) measurements of the Na_xWO_3 metamaterials, with increasing Na/W ratio from 0.2 to 1. A strong peak at 0 eV is attributed to the zero-loss energy and is intrinsic of EELS measurements. Consistent with the theoretical transition energies, the broad peak associated to the discussed interband contributions (Figure 3a, light yellow box) becomes visible at around ~3 eV and gets more pronounced at ~4 eV. Increasing the Na/W ratio, and thus metallicity, increases the interband-peak width. A strong loss due to the intraband transitions is present at around 2 eV for any Na/W ratio equal or above 0.4 (Figure 3a, light blue region), further confirming that a metallic material behaviour above the MIT Na threshold ratio. The 2 eV characteristic peak is absent for lower Na concentration, indicating a semiconductor behaviour[35, 45].

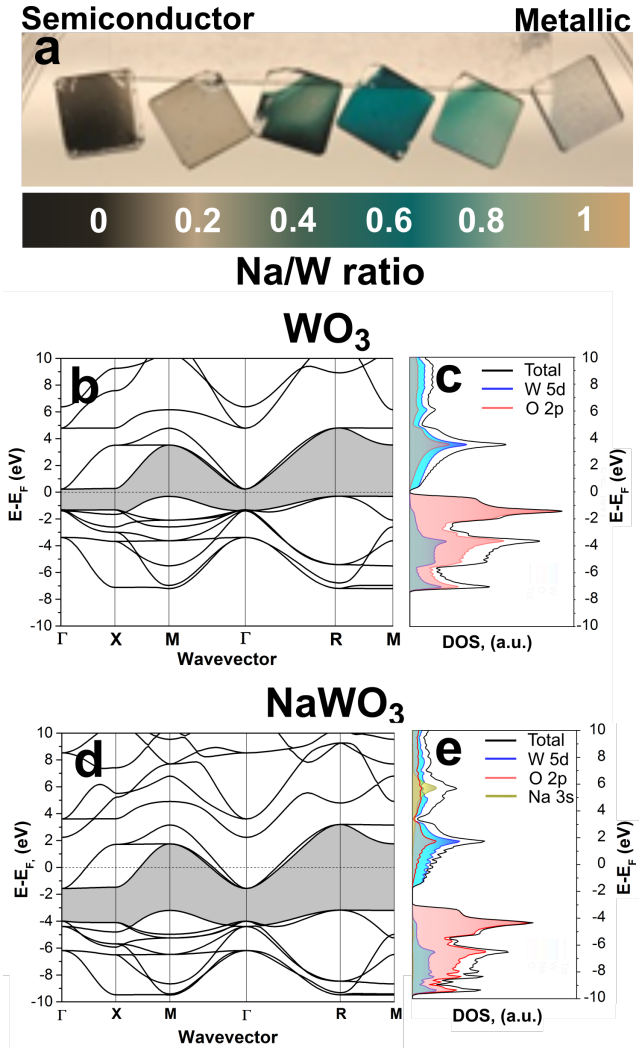

Figure 2. a) Optical images of Na_xWO_3 metamaterials as a function of the Na/W ratio from 0 to 1. b-e) Computed band structure and density of the states for the representative semiconductor (b,c) WO_3 and metallic (d,e) $NaWO_3$ systems.

A set of complementary characterization was pursued to confirm the MIT transition threshold and evolution of the Na_xWO_3 structural and optoelectronic properties (see also Supplementary Information S2-S6). X-ray powder diffraction (XRD) measurements show that reduction of the pure WO_3 nanoparticle networks leads to formation of WO_2 (Figure 3b). Increasing Na/W ratio decreases the WO_2 peak intensity and show the formation of an increasing amount of Na_xWO_3 phase with space group Pm-3m. At Na/W ratio above 0.4, a pure Na_xWO_3 phase is obtained with no trace of WO_2 crystals. Further characterization on the crystallinity and uniformity is shown in Supplementary Information S2 and S3. These results indicate that the Na ions intercalate in the WO_3 lattice during the reduction, leading to the formation of a stable, and eventually pure Na_xWO_3 phase.

Figure 3c shows UV-Vis transmittance as a function of the Na/W ratio. Sodium ratios below 0.4 display a low and flat transmittance across the whole visible spectrum, attributed to the small bandgap (~0.6 eV) of the WO_2.[33] At a Na/W ratio of 0.4, a broad transmittance peak appears in the wavelength range of 450 - 650 nm, further indicating that a MIT transition is obtained at this threshold sodium content. Increasing the Na/W ratio above 0.4 increases and sharpens this transmittance peak. Notably, a Na/W ratio of 0.6 ($Na_{0.6}WO_3$) leads to the

highest transmittance band and quality factor, making it a promising candidate for use in optical sensing.

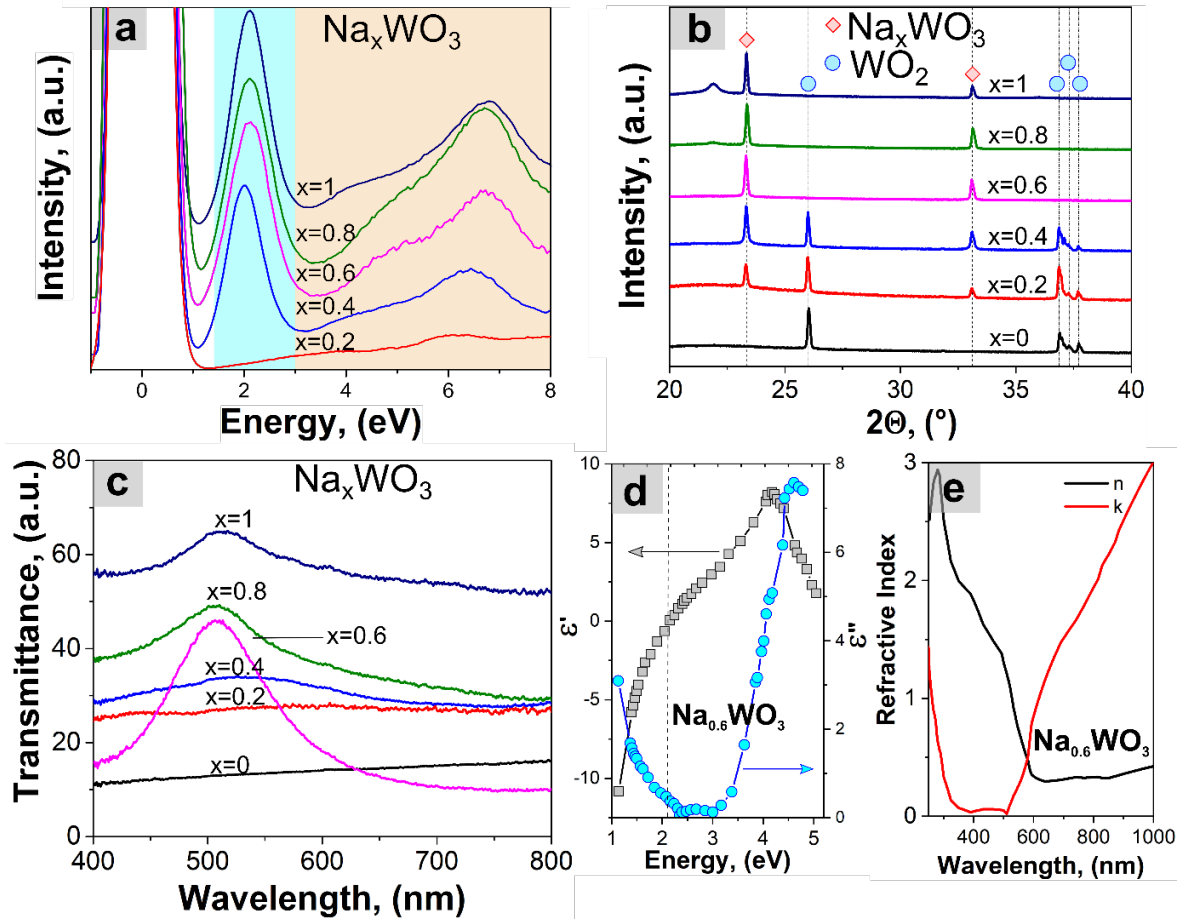

Figure 3. a) EELS measurements of the Na_xWO_3 metamaterials as a function of the Na/W ratio, showing contributions of intraband (light blue region) and interband (light yellow region) transitions. b-c) XRD patterns and UV-Vis transmittance measurements of the Na_xWO_3 metamaterials at the same Na/W ratios. d-e) Real (ε') and imaginary part (ε") of the permittivity and refractive index (n,k) for $Na_{0.6}WO_3$, respectively, taken from Ref [46]. The dotted line in panel d represents the ENZ condition.

Figure 3d shows the real and imaginary component of the permittivity (ε' and ε") for $Na_{0.6}WO_3$. At this Na/W ratio, ε' vanishes at ~2.1 eV (~ 590 nm) demonstrating an epsilon-near-zero window in this spectral range. As the causality condition forbids the possibility to have lossless and negative permittivity simultaneously in any dispersive material,[47] the imaginary part ε" is close to zero (< 0.5) indicating low losses within this energy region. By using the known square-root relationship, we computed the refractive index components for $Na_{0.6}WO_3$ (Figure 3e). The imaginary part, k, of the refractive index shows intraband losses arising from free-electrons –predominantly at high wavelengths– and from interband transitions –predominantly at low wavelengths– while between 400 to 600 nm, k is always less than unity, corroborating the low-loss behaviour. Interestingly, at ~515 nm, $Na_{0.6}WO_3$ shows a real part of the refractive index close to the unity; this wavelength matches well the transmission peak wavelength (Figure 3c), indicating that the transmission maximum results from a matched effective permittivity of the metamaterial to the surrounding environment.
To gain further insights into the interaction of these Na_xWO_3 metamaterials with light, we have performed a set of finite-difference time domain approach (FDTD) simulations (see

Methods in Supplementary Information). Figure 4a shows the electric field enhancement ($\mathbf{E/E_0}$) on a vertical cross-sectional plane through the middle of the cube as a function of wavelength. At wavelengths of ca. 300 nm, a first enhancement attributed to interband transitions is observed within the cube bulk. Interestingly, in a broad range of frequencies, between ~450 and 600 nm, the electric field enhancement has a constant spatial field distribution in the medium. Figure 4b shows a *y-z* cross-section of the cube at a wavelength of 523 nm, which shows a unitary field-enhancement indicating that the $Na_{0.6}WO_3$ cube is essentially invisible at these wavelengths due to impedance matching with the surrounding medium. At wavelengths above 600 nm, the near-field is increasingly enhanced. The $\mathbf{E/E_0}$ reaches its peak values in the NIR range at the interfaces of the cube with the air and substrate. This is attributed to the light absorption by free carriers and the excitation of localized surface plasmon polaritons[48].

Figure 4 c-e shows computed scattering cross-sections, σ_{scatt}, for different morphologies, including cubic, spherical and hexagonal polygons. The σ_{scatt} is determined by two major bands, one in the high energy region (200-400 nm) which corresponds to the absorption due to the interband transitions at the plasma frequency and a second one above ~700 nm which corresponds to the excitation of free carriers by intraband transition[49]. Remarkably, the scattering minimum at λ~520 nm, arising from a refractive index close to 1, is almost entirely independent of the geometry and particle size.

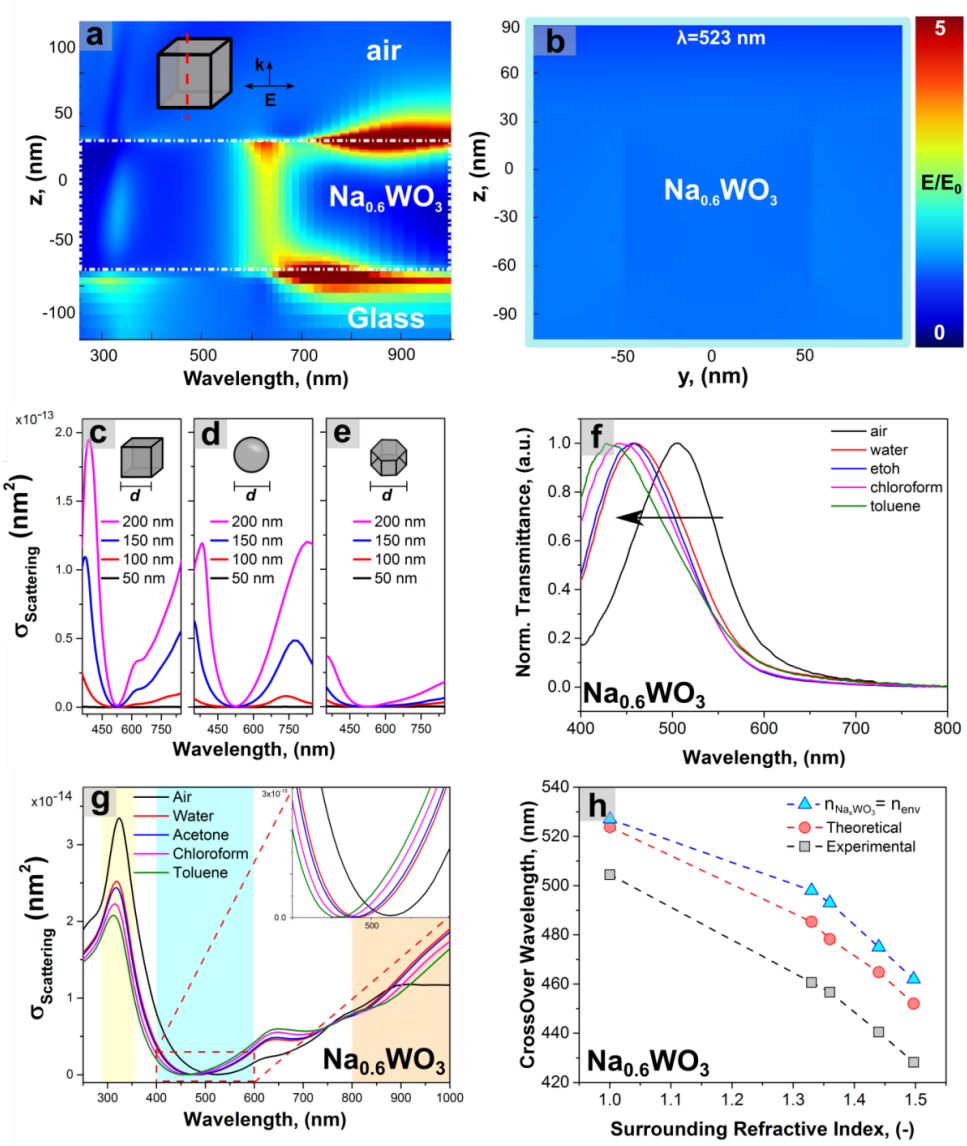

Figure 4. a) Chromatic map showing the electric field enhancement (**E/E₀**) as a function of the wavelength for a $Na_{0.6}WO_3$ cube with a 100 nm edge placed between -70 < *z* < +30 delimited by the white dotted line and taken at the edge of the cube (dotted red line in the inset) b) Orthogonal cross-section image of the *y*-*z* plane showing the unitary field enhancement at a wavelength of 523 nm. c-e) Scattering cross-section for $Na_{0.6}WO_3$ crystals having different shapes (cubic, spherical and hexagonal polygon, respectively) and dimensions, ranging from 50 to 200 nm. f) Normalized transmittance measurements of the $Na_{0.6}WO_3$ metamaterials with increasing environment refractive indexes (RI). g) Computed scattering cross-section for a $Na_{0.6}WO_3$ crystal as a function of the environment RIh) Experimental and computed cross-over wavelength blueshift as a function of the environment RI.

We demonstrate the use of the relatively inert, in terms of intra- and inter-band transitions, region of the Na_xWO_3 metamaterials to develop a non-resonant sensing approach. Notably, we observed that, by exposing the $Na_{0.6}WO_3$ metamaterials to environments having an increasing refractive index (n_{env}), the transmittance peak blueshifts toward smaller wavelengths (Figure 4f). Specifically, increasing the refracting index from air (~1) to toluene (1.49) the transmittance peak maximum blueshifts by about 100 nm, from ~510 nm to ~420 nm. This corresponds to a large refractive index sensitivity of 150 nm/RIU. This novel

sensing mechanism provide an interesting alternative for monitoring refractive index changes with high sensitivity. Indeed, our device compares favourably against other label-free nanoparticle-based plasmonic[50]and dielectric sensing platforms[51], as well as against slot-waveguide RI sensors[52] and 2D photonic crystals. For instance, our device shows a threefold enhancement with respect to the sensitivity (~50 nm/RIU) of plasmonic Au nanospheres[53] and more than the double of silver-coated optical fiber plasmonic sensors.[54] While other platforms have achieved higher performances[55], they often require challenging geometrical optimization strategies or time-consuming functionalization processes. In contrast, the facile synthesis process and the structure-independent sensing mechanism of our Na_xWO_3 metamaterials could be favourable in contexts where cost and scalability are important.

To gain insights on this sensing mechanism, we have computed the scattering cross-section of $Na_{0.6}WO_3$ crystals as a function of the environment refractive index (Figure 4g). Increasing the surrounding refractive index of the medium from 1 to 1.49, decreases the $Na_{0.6}WO_3$ scattering in the UV region. While the computed NIR plasmonic resonance red-shifts with increasing n_{env}, the wavelength where the scattering cross-section is minimized blue-shifts (Figure 4h, red circles). This trend is in very good agreement with the experimental measurements revealing a blueshift of the transmission peak maximum with increasing refractive index (Figure 4h, grey squares).

We provide an explanation of this interesting phenomenon proposing a refractive index matching mechanism. Within the Mie scattering theory, the wavelength where the transmission is maximum, and where the scattering is lowest, corresponds to the wavelength, where the refractive index of the $Na_{0.6}WO_3$ crystal is equal to the real part of the refractive index of the environment, resulting in a matching condition. Considering that the real part of the $Na_{0.6}WO_3$ refractive index (n) increases from 1 to 1.49 with decreasing wavelength from 527 to 462 nm (Figure 3e), the index-matching condition shifts to shorter wavelengths when the surrounding refractive index increases (Figure 4h, triangles). This matching condition is in agreement with the computed blueshift of the scattering cross-section as a function of environment refractive index (Figure 4h, circles) and shows a good consistency with the measured blueshift (Figure 4h, square). To the best of our knowledge, this is the first demonstration of non-resonant, size- and shape- independent refractive index matching based on impedance matching.

Conclusions

We presented the engineering of epsilon-near-zero Na_xWO_3 metamaterials with tuneable optoelectronic properties by the large-scale self-assembly and reduction of flame-made Na_x-WO_3 nanoparticles. We exploited the intercalation Na in the WO_3 lattices to induce a metal-to-insulator transition, resulting in epsilon-near-zero properties at visible wavelengths. Our first principle and FTDT simulations, and experimental characterizations indicate a structural independent ENZ region at visible wavelengths, providing a robust and facile mean for the preparation of tailored ENZ materials. We explore the use of these non-periodic Na_xWO_3 metamaterials for optical sensing, demonstrating a non-resonant sensing mechanism based on the refractive index matching, with sensitivities as high as 150 nm/RIU. This is a threefold enhancement with respect to the sensitivity of plasmonic Au nanospheres, while simultaneously drastically reducing radiation losses. We believe that these novel insights and the unique properties of these tuneable Na_xWO_3 metamaterials provide a promising family of optical materials for the engineering of optoelectronic devices with application extending from sensing and light harvesting to photocatalysis and optical clocking.

Acknowledgments

This research was funded by and has been delivered in partnership with Our Health in Our Hands (OHIOH), a strategic initiative of the Australian National University, which aims to transform healthcare by developing new personalised health technologies and solutions in collaboration with patients, clinicians, and health care providers. AT acknowledges financial support from the North Atlantic Treaty Organization Science for Peace and Security Programme project AMOXES (#G5634). The authors would like to thank the precious advices given by Prof. Dragomir Neshev and Dr. Mohsen Rahmani, who provided helpful suggestions needed for the development of the project. All the authors acknowledge the use of the Australian National Fabrication Facility (ANFF), ACT Node, as well as the Centre of Advanced Microscopy (CAM) at ANU.

Supporting Information

Supporting information include detailed procedure and methods for the material synthesis as well as further characterization of the morphological and optoelectronic properties achieved via scanning transmission electron microscopy, photoluminescence, and TEM. Additionally, the Drude model and the contribution of interband and intraband transition is explained in the appendix.

References

1. Stockman, M. I. Nanoplasmonics: The physics behind the applications. *Physics Today* **2011,** 64, (2), 39-44.
2. Liu, N.; Tang, M. L.; Hentschel, M.; Giessen, H.; Alivisatos, A. P. Nanoantenna-enhanced gas sensing in a single tailored nanofocus. *Nature Materials* **2011,** 10, 631.
3. Khurgin, J. B. How to deal with the loss in plasmonics and metamaterials. *Nature Nanotechnology* **2015,** 10, 2.
4. Anker, J. N.; Hall, W. P.; Lyandres, O.; Shah, N. C.; Zhao, J.; Van Duyne, R. P. Biosensing with plasmonic nanosensors. *Nature Materials* **2008,** 7, 442.
5. Fusco, Z.; Rahmani, M.; Bo, R.; Verre, R.; Motta, N.; Käll, M.; Neshev, D.; Tricoli, A. Nanostructured Dielectric Fractals on Resonant Plasmonic Metasurfaces for Selective and Sensitive Optical Sensing of Volatile Compounds. *Advanced Materials* **2018,** 30, (30), 1800931.
6. Kelly, K. L.; Coronado, E.; Zhao, L. L.; Schatz, G. C. The Optical Properties of Metal Nanoparticles: The Influence of Size, Shape, and Dielectric Environment. *The Journal of Physical Chemistry B* **2003,** 107, (3), 668-677.
7. Ross, M. B.; Mirkin, C. A.; Schatz, G. C. Optical Properties of One-, Two-, and Three-Dimensional Arrays of Plasmonic Nanostructures. *The Journal of Physical Chemistry C* **2016,** 120, (2), 816-830.
8. Fusco, Z.; Rahmani, M.; Bo, R.; Tran-Phu, T.; Lockrey, M.; Motta, N.; Neshev, D.; Tricoli, A. High-Temperature Large-Scale Self-Assembly of Highly Faceted Monocrystalline Au Metasurfaces. *Advanced Functional Materials* **2019,** 29, (2), 1806387.
9. Fusco, Z.; Bo, R.; Wang, Y.; Motta, N.; Chen, H.; Tricoli, A. Self-assembly of Au nano-islands with tuneable organized disorder for highly sensitive SERS. *Journal of Materials Chemistry C* **2019**.
10. Khurgin, J. B.; Boltasseva, A. Reflecting upon the losses in plasmonics and metamaterials. *MRS Bulletin* **2012,** 37, (8), 768-779.
11. West, P. R.; Ishii, S.; Naik, G. V.; Emani, N. K.; Shalaev, V. M.; Boltasseva, A. Searching for better plasmonic materials. *Laser & Photonics Reviews* **2010,** 4, (6), 795-808.
12. Lee, D. E.; Lee, Y. J.; Shin, E.; Kwon, S.-H. Mach-Zehnder Interferometer Refractive Index Sensor Based on a Plasmonic Channel Waveguide. *Sensors* **2017,** 17, (11), 2584.
13. Sreekanth, K. V.; Alapan, Y.; ElKabbash, M.; Ilker, E.; Hinczewski, M.; Gurkan, U. A.; De Luca, A.; Strangi, G. Extreme sensitivity biosensing platform based on hyperbolic metamaterials. *Nat Mater* **2016,** 15, (6), 621-7.
14. Lee, D. E.; Lee, T.-W.; Kwon, S.-H. Spatial mapping of refractive index based on a plasmonic tapered channel waveguide. *Optics Express* **2015,** 23, (5), 5907-5914.
15. Rarity, J. G.; Tapster, P. R.; Jakeman, E.; Larchuk, T.; Campos, R. A.; Teich, M. C.; Saleh, B. E. A. Two-photon interference in a Mach-Zehnder interferometer. *Physical Review Letters* **1990,** 65, (11), 1348-1351.
16. Niu, X.; Hu, X.; Chu, S.; Gong, Q. Epsilon-Near-Zero Photonics: A New Platform for Integrated Devices. *Advanced Optical Materials* **2018,** 6, (10), 1701292.
17. Rensberg, J.; Zhou, Y.; Richter, S.; Wan, C.; Zhang, S.; Schöppe, P.; Schmidt-Grund, R.; Ramanathan, S.; Capasso, F.; Kats, M. A.; Ronning, C. Epsilon-Near-Zero Substrate Engineering for Ultrathin-Film Perfect Absorbers. *Physical Review Applied* **2017,** 8, (1), 014009.

18. Jun, Y. C.; Reno, J.; Ribaudo, T.; Shaner, E.; Greffet, J.-J.; Vassant, S.; Marquier, F.; Sinclair, M.; Brener, I. Epsilon-Near-Zero Strong Coupling in Metamaterial-Semiconductor Hybrid Structures. *Nano Letters* **2013,** 13, (11), 5391-5396.
19. Engheta, N. Circuits with Light at Nanoscales: Optical Nanocircuits Inspired by Metamaterials. *Science* **2007,** 317, (5845), 1698-1702.
20. Adams, D. C.; Inampudi, S.; Ribaudo, T.; Slocum, D.; Vangala, S.; Kuhta, N. A.; Goodhue, W. D.; Podolskiy, V. A.; Wasserman, D. Funneling Light through a Subwavelength Aperture with Epsilon-Near-Zero Materials. *Physical Review Letters* **2011,** 107, (13), 133901.
21. Alù, A.; Engheta, N. Achieving transparency with plasmonic and metamaterial coatings. *Physical Review E* **2005,** 72, (1), 016623.
22. Alam, M. Z.; De Leon, I.; Boyd, R. W. Large optical nonlinearity of indium tin oxide in its epsilon-near-zero region. *Science* **2016,** 352, (6287), 795-797.
23. Maas, R.; Parsons, J.; Engheta, N.; Polman, A. Experimental realization of an epsilon-near-zero metamaterial at visible wavelengths. *Nature Photonics* **2013,** 7, (11), 907-912.
24. Lee, Y. U.; Garoni, E.; Kita, H.; Kamada, K.; Woo, B. H.; Jun, Y. C.; Chae, S. M.; Kim, H. J.; Lee, K. J.; Yoon, S.; Choi, E.; Mathevet, F.; Ozerov, I.; Ribierre, J. C.; Wu, J. W.; D'Aléo, A. Strong Nonlinear Optical Response in the Visible Spectral Range with Epsilon-Near-Zero Organic Thin Films. *Advanced Optical Materials* **2018,** 6, (14), 1701400.
25. Adams, D. C.; Inampudi, S.; Ribaudo, T.; Slocum, D.; Vangala, S.; Kuhta, N. A.; Goodhue, W. D.; Podolskiy, V. A.; Wasserman, D. Funneling light through a subwavelength aperture with epsilon-near-zero materials. *Phys Rev Lett* **2011,** 107, (13), 133901.
26. Naik, G. V.; Shalaev, V. M.; Boltasseva, A. Alternative plasmonic materials: beyond gold and silver. *Adv Mater* **2013,** 25, (24), 3264-94.
27. Pacheco-Peña, V.; Engheta, N.; Kuznetsov, S.; Gentselev, A.; Beruete, M. Experimental Realization of an Epsilon-Near-Zero Graded-Index Metalens at Terahertz Frequencies. *Physical Review Applied* **2017,** 8, (3), 034036.
28. Luo, J.; Xu, P.; Gao, L. Directive emission based on one-dimensional metal heterostructures. *J. Opt. Soc. Am. B* **2012,** 29, (1), 35-39.
29. Alù, A.; Engheta, N. Light squeezing through arbitrarily shaped plasmonic channels and sharp bends. *Physical Review B* **2008,** 78, (3), 035440.
30. Raj, S.; Matsui, H.; Souma, S.; Sato, T.; Takahashi, T.; Chakraborty, A.; Sarma, D. D.; Mahadevan, P.; Oishi, S.; McCarroll, W. H.; Greenblatt, M. Electronic structure of sodium tungsten bronzesNaxWO3by high-resolution angle-resolved photoemission spectroscopy. *Physical Review B* **2007,** 75, (15).
31. Raub, C. J.; Sweedler, A. R.; Jensen, M. A.; Broadston, S.; Matthias, B. T. Superconductivity of Sodium Tungsten Bronzes. *Physical Review Letters* **1964,** 13, (25), 746-747.
32. Guo, C.; Yin, S.; Huang, L.; Sato, T. Synthesis of One-Dimensional Potassium Tungsten Bronze with Excellent near-Infrared Absorption Property. *ACS Applied Materials & Interfaces* **2011,** 3, (7), 2794-2799.
33. Cui, G.; Wang, W.; Ma, M.; Xie, J.; Shi, X.; Deng, N.; Xin, J.; Tang, B. IR-Driven Photocatalytic Water Splitting with WO2-NaxWO3 Hybrid Conductor Material. *Nano Lett* **2015,** 15, (11), 7199-203.
34. Huibregtse, E. J.; Barker, D. B.; Danielson, G. C. Electrical Properties of Sodium Tungsten Bronze. *Physical Review* **1951,** 84, (1), 142-144.
35. Tegg, L.; Cuskelly, D.; Keast, V. J. Plasmon Responses in the Sodium Tungsten Bronzes. *Plasmonics* **2017,** 13, (2), 437-444.
36. Tegg, L.; Cuskelly, D.; Keast, V. J. Bulk scale fabrication of sodium tungsten bronze nanoparticles for applications in plasmonics. *Nanotechnology* **2018,** 29, (40), 40LT02.
37. Tegg, L.; Cuskelly, D.; Keast, V. J. The sodium tungsten bronzes as plasmonic materials: fabrication, calculation and characterization. *Materials Research Express* **2017,** 4, (6).

38. Kosov, A. V.; Semerikova, O. L.; Vakarin, S. V.; Pankratov, A. A.; Plaksin, S. V.; Korzun, I. V.; Akashev, L. A.; Zaykov, Y. P. Electrochemical synthesis of tetragonal oxide tungsten bronze nanofilms on platinum. *Russian Metallurgy (Metally)* **2017,** 2017, (2), 152-157.
39. Li, X.; Xie, R.; Cao, X.; Liu, L.; Xu, L.; Wang, Y.; Meng, C.; Wu, Q. Synthesis of cubic sodium tungsten bronze NaxWO3 in air. *Journal of the American Ceramic Society* **2018,** 101, (10), 4458-4462.
40. Nasiri, N.; Elmoe, T. D.; Liu, Y.; Qin, Q. H.; Tricoli, A. Self-assembly dynamics and accumulation mechanisms of ultra-fine nanoparticles. *Nanoscale* **2015,** 7, (21), 9859-67.
41. Nasiri, N.; Bo, R.; Hung, T. F.; Roy, V. A. L.; Fu, L.; Tricoli, A. Tunable Band-Selective UV-Photodetectors by 3D Self-Assembly of Heterogeneous Nanoparticle Networks. *Advanced Functional Materials* **2016,** 26, (40), 7359-7366.
42. Hollinger, G.; Pertosa, P.; Doumerc, J. P.; Himpsel, F. J.; Reihl, B. Metal-nonmetal transition in tungsten bronzes: A photoemission study. *Physical Review B* **1985,** 32, (4), 1987-1991.
43. Hjelm, A.; Granqvist, C. G.; Wills, J. M. Electronic structure and optical properties of WO3, LiWO3, NaWO3, and HWO3. *Physical Review B* **1996,** 54, (4), 2436-2445.
44. Ingham, B.; Hendy, S. C.; Chong, S. V.; Tallon, J. L. Density-functional studies of tungsten trioxide, tungsten bronzes, and related systems. *Physical Review B* **2005,** 72, (7).
45. Kielwein, M.; Saiki, K.; Roth, G.; Fink, J.; Paasch, G.; Egdell, R. G. High-energy electron-energy-loss study of sodium-tungsten bronzes. *Physical Review B* **1995,** 51, (16), 10320-10335.
46. Owen, J. F.; Teegarden, K. J.; Shanks, H. R. Optical properties of the sodium-tungsten bronzes and tungsten trioxide. *Physical Review B* **1978,** 18, (8), 3827-3837.
47. Dressel, M.; Gruener, G. Electrodynamics of Solids: Optical Properties of Electrons in Matter. *American Journal of Physics* **2002,** 70, (12), 1269-1270.
48. Mattox, T. M.; Bergerud, A.; Agrawal, A.; Milliron, D. J. Influence of Shape on the Surface Plasmon Resonance of Tungsten Bronze Nanocrystals. *Chemistry of Materials* **2014,** 26, (5), 1779-1784.
49. Xue, Y.; Zhang, Y.; Zhang, P. Theory of the color change ofNaxWO3as a function of Na-charge doping. *Physical Review B* **2009,** 79, (20).
50. Lin, Y. Z., Y.; Mo, Y.; Guo, J.; Lindquist, R.G. . E-Beam Patterned Gold Nanodot Arrays on Optical Fiber Tips for Localized Surface Plasmon Resonance Biochemical Sensing. *Sensors* **2010** 10, 9397-9406.
51. Yildirim, D. U.; Ghobadi, A.; Soydan, M. C.; Gokbayrak, M.; Toprak, A.; Butun, B.; Ozbay, E. Colorimetric and Near-Absolute Polarization-Insensitive Refractive-Index Sensing in All-Dielectric Guided-Mode Resonance Based Metasurface. *The Journal of Physical Chemistry C* **2019,** 123, (31), 19125-19134.
52. Barrios, C. A.; Gylfason, K. B.; Sánchez, B.; Griol, A.; Sohlström, H.; Holgado, M.; Casquel, R. Slot-waveguide biochemical sensor. *Opt. Lett.* **2007,** 32, (21), 3080-3082.
53. Chen, H.; Kou, X.; Yang, Z.; Ni, W.; Wang, J. Shape- and Size-Dependent Refractive Index Sensitivity of Gold Nanoparticles. *Langmuir* **2008,** 24, (10), 5233-5237.
54. Ortega-Mendoza, J. G.; Padilla-Vivanco, A.; Toxqui-Quitl, C.; Zaca-Morán, P.; Villegas-Hernández, D.; Chávez, F. Optical fiber sensor based on localized surface plasmon resonance using silver nanoparticles photodeposited on the optical fiber end. *Sensors (Basel, Switzerland)* **2014,** 14, (10), 18701-18710.
55. Xu, Y.; Bai, P.; Zhou, X.; Akimov, Y.; Png, C. E.; Ang, L.-K.; Knoll, W.; Wu, L. Optical Refractive Index Sensors with Plasmonic and Photonic Structures: Promising and Inconvenient Truth. *Advanced Optical Materials* **2019,** 7, (9), 1801433.